Dislocation cells in additively manufactured metallic alloys characterized by electron backscatter diffraction pattern sharpness

Fulin Wang^{a,b,1}, Jean-Charles Stinville^c, Marie Charpagne^c, McLean P. Echlin^b, Sean R. Agnew^d, Tresa M. Pollock^b, Marc De Graef^e, Daniel S. Gianola^{b,1}

^aNational Engineering Research Center of Light Alloy Net Forming, School of Materials Science and Engineering, Shanghai Jiao Tong University, Shanghai, China

^bMaterials Department, University of California Santa Barbara, Santa Barbara, USA
 ^cDepartment of Materials Science and Engineering, University of Illinois at Urbana-Champaign, Urbana, USA
 ^dDepartment of Materials Science and Engineering, University of Virginia, Charlottesville, VA, USA
 ^eDepartment of Materials Science and Engineering, Carnegie Mellon University, Pittsburgh, PA, USA

Abstract

Metallic alloys produced by additive manufacturing often host complex and hierarchical microstructures with grains exhibiting large orientation gradients, along with sub-grain dislocation cells. These multiscale features act in concert to control mechanical behavior, yet are challenging to characterize at high fidelity over large areas. Here, we quantify the sharpness of electron backscatter diffraction patterns obtained from several additively manufactured metallic alloys, to reveal the dislocation cells at the mesoscale in bulk materials. The sharpness metric used reflects the elastic strain field from dislocations, and exhibits unique advantages, including being proportional to local dislocation density, insensitive to grain orientation, and inherently correlated with orientation mapping modality and alike. Our results demonstrate that the cell walls do not always possess appreciable misorientations, and thus do not always contain large fraction of geometrically necessary dislocations, thereby furthering our understanding of the origin and implications of the profuse dislocation cells produced during additive manufacturing.

Keywords: electron backscattering diffraction (EBSD); dislocation cell; metal and alloys; microstructure; additive manufacturing.

1. Introduction

Additively manufactured (AM) metallic materials possess microstructures that span multiple length scales, from columnar grains that approach 100 micrometers long to equiaxed grains whose diameters are tens of micrometers [1-3]. Moreover, it is generally acknowledged that the as-built materials often contain profuse submicrometer dislocation cells, and that they are the determining structural motifs that govern the strength and ductility of AM materials [4-8]. Achieving the goal of incorporating all salient elements of a multiscale microstructure into a predictive mechanical model of AM materials requires the ability to characterize the full and often complex landscape of the microstructure, e.g. periodicity of the melt pools, nature of the dislocation cells at high spatial resolution. Furthermore, dislocation cells often exhibit morphologies that depend on the parent grain orientation and are related to local misorientations [4, 5], thereby necessitating both imaging and quantitative mea-

Transmission electron microscopy (TEM) is the most commonly used method to characterize dislocations, and can be integrated with energy-dispersive spectroscopy (EDS) mapping, and orientation mapping using transmission Kikuchi diffraction

(TKD) or precession electron diffraction (PED) [4, 9] to develop a correlative understanding of the cell walls with chemical segregation and local misorientation. Other techniques, such as electron channeling contrast imaging (ECCI) [10] and imaging of etched surfaces [6] in a scanning electron microscope (SEM) have also been employed, which are able to inspect substantially larger areas than TEM-based methods and thus can provide microstructural statistics that are otherwise not available. These SEM imaging modalities are often coupled with crystallographic orientation maps obtained by electron backscatter diffraction (EBSD), allowing the descriptions of cells in terms of their sizes, morphology, and misorientation gradients. However, high resolution definition of the cell structure, such as is available by TEM, while spanning many grains, is lacking, leaving certain aspects of the cell structure shrouded in mystery. For instance, while intuitively the tangled dislocation cell walls may correspond to low angle grain boundaries, in 316L stainless steel (SS) produced by powder-bed selective laser melting (SLM), the walls were shown to delineate regions of distinct orientations [9], yet they were also characterized to exhibit kernel average misorientation (KAM) values below 1°, and the walls do not clearly coincide with high KAM lines [4]. A single characterization technique capable of providing both crystal orientation and sub-grain defect information that spans the length scales of additively manufactured materials, promises to accelerate the materials design and testing cycles.

 $[\]begin{tabular}{ll} *corresponding authors: full inwang@sjtu.edu.cn (F.W.), gianola@ucsb.edu (D.S.G.) \end{tabular}$

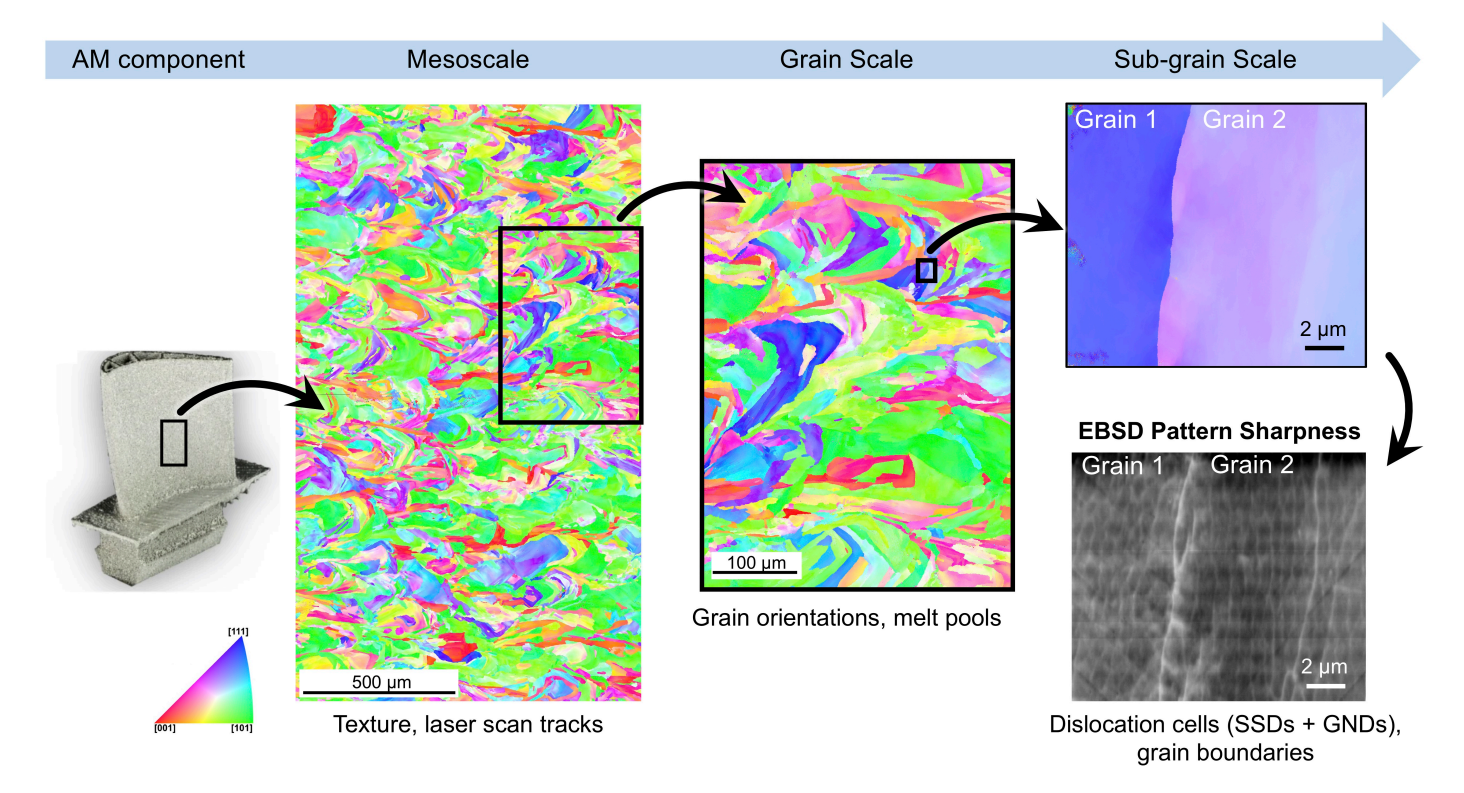


Figure 1: (left) EBSD scan maps, here shown as inverse pole figure (IPF) orientation maps, are routinely collected from component-relevant mesoscale (several mm²) areas where microstructural heterogeneities, prevalent in AM materials, are quantified. (right) The total dislocation content, including both SSDs and GNDs, are captured collectively using the EBSD pattern sharpness metric. Note that the GNDs alone can be extracted from the same EBSD dataset using methods described elsewhere [1]]. It is note-worthy that dislocation cell contrast in the pattern sharpness map is preserved across grains at different crystal orientations, i.e. the contrast is not sensitive to the local diffraction condition.

Moreover, an approach that gives the total dislocation content, including both geometrically necessary (GND) and statistically stored dislocation (SSD) would signify a substantial advance.

In this work, we characterized dislocation cells in AM microstructures using EBSD methods. Specifically, the sharpness of the EBSD pattern was employed as a metric to reflect the extent of dislocations within the volume probed by the electron beam while scanning the material. Three SLM printed metallic materials were investigated: 316L SS, Inconel 625 Ni-base superalloy, and SB-CoNi-10 CoNi-base superalloy. The microstructure of all three as-printed alloys can be broadly described as having large grains that contain varying sub-grain orientation spread. The pattern sharpness metric captures the thickness of the dislocation cells and maintains contrast across subgrain regions that vary in misorientation, as well as across low and high angle grain boundaries. Pattern sharpness combined with other EBSD analysis approaches provides a route for the scaling of characterization of additive and other dislocation defect structures from the mesoscale to the sub-micron scale.

2. Methods

SLM printed samples of Inconel 625 Ni-base superalloy, and SB-CoNi-10 CoNi-base superalloy were obtained from a variety of printers and conditions. The printing parameters for

each of the samples are detailed in [5] [12-15]. All these materials and print conditions are known to produce dislocation cell structures.

EBSD characterization was performed on a Versa 3D SEM (Thermo Fisher Scientific) equipped with a Hikari Plus EBSD detector (EDAX), and an Apreo S SEM (Thermo Fisher Scientific) equipped with a custom built direct electron detector (DED, Direct Electron) that has high electron detection sensitivity and was operated at 1024×1024 resolution, ensuring high quality patterns [16]. Raw EBSD patterns were collected for all detectors and were stored in both the HDF data format and UP2 binary file format.

While the sharpness of a pattern can be qualitatively assessed from the logarithmic power spectrum, a sharpness metric can be calculated according to the formulae of Lassen [17], as adopted in the open-source EBSD simulation and indexing programs EMsoft and EMSphInx [18] [19], as well as the EBSD data processing and analysis Python library kikuchipy [20]. The sharpness of a pattern is defined as the second moment of its power spectrum (variance of the spherically-averaged distribution of spatial frequencies). Therefore, sharper Kikuchi bands have greater high frequency content in the power spectrum with sharpness values closer to unity. It should be noted that in these programs where Hough transforms are not used for indexing, there is no Hough-based image quality (as in the EDAX software). Accordingly, the calculated pattern sharpness value is

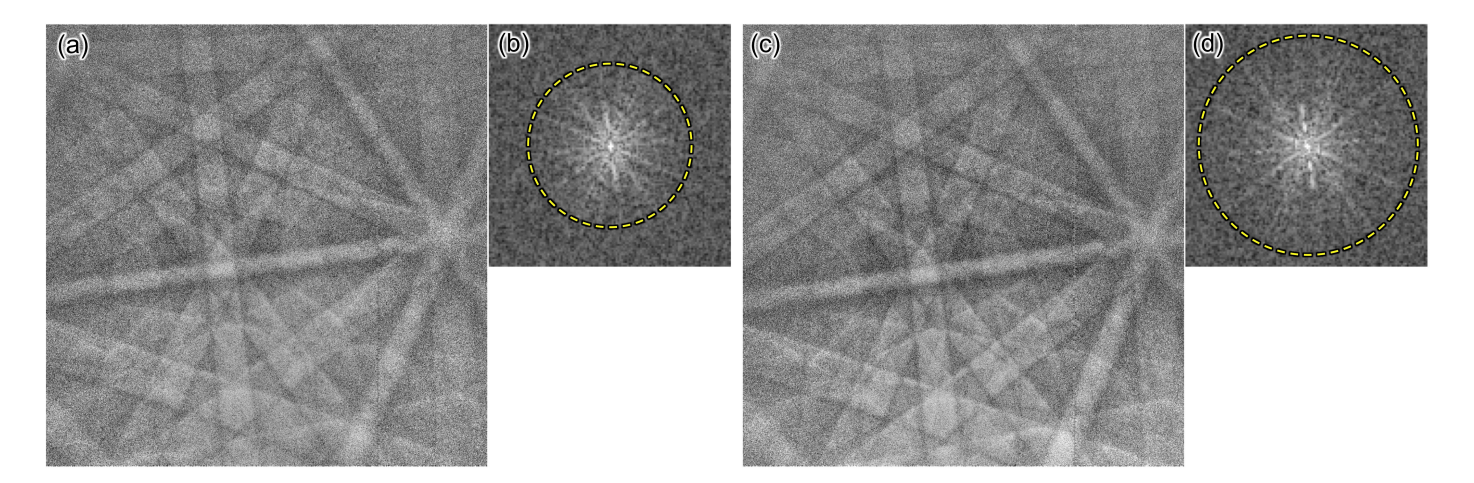


Figure 2: (a) and (c) are experimental patterns collected from nearby a dislocation cell wall and far away from a cell wall, but within the same grain. The patterns were acquired with the DED with an accelerating voltage of 20 kV, 13 nA electron beam current, 55 fps detector acquisition speed, and with a detector resolution of 1024×1024 pixels. (b) and (d) are the corresponding logarithmic power spectra of (a) and (c).

given as the image quality parameter. In the present study, the sharpness metric is generated from EMSphInx.

3. Results and Discussion

Fig. II demonstrates a workflow for the collection and analysis of EBSD data across the length scales that are relevant to AM materials. At the mesoscale, the overall texture and solidification structure are evident, while at the grain-scale specific crystallographic orientations and melt pool artifacts are visible. Pattern sharpness provides a measurement into the sub-grain scale where individual dislocation cells can be resolved in relation to sub-grain orientation gradients and low and high angle grain boundaries. The dislocation cell wall contrast is maintained across high angle grain boundaries, a unique advantage compared to other imaging methods of dislocation structure that are sensitive to the local diffraction condition and hence require a series of specimen tilting and imaging steps to maintain/optimize contrast as the crystal orientation being probed varies.

The quality of the EBSD diffraction pattern is frequently used to highlight crystalline defects, including grain boundaries and a high density of dislocations [21]. Specifically for the latter, the strain field of a group of dislocations perturbs the local diffracting lattice planes, leading to incoherent scattering and thus degrading the diffraction pattern. One way to define the image quality (IQ) of an EBSD pattern, as used in the EDAX EBSD software, is to calculate the sum of the peak magnitudes in the Hough transformation of the pattern [22, 23]. In this regard, it is approximately proportional to the intensity (or height) of the diffraction bands.

The breadth of the diffraction signal, the principle that underlies X-ray diffraction (XRD) peak broadening analysis, has been quantitatively related to dislocation densities in bulk materials in work by those such as Ungar et al. [24, 25]. In specimens containing higher dislocation densities, the diffraction peak becomes broader and less sharp, regardless of the peak

intensity. Recently, a similar concept was applied to the analysis of EBSD patterns to describe the sharpness of the Kikuchi band edges [26]. By performing dynamical electron scattering calculations on a diffracting volume with varying amounts of artificially introduced dislocations, the sharpness of the EBSD pattern was demonstrated to be inversely proportional to dislocation density across the range of roughly 10^{14} to 10^{16} m⁻². The lower limit of this density reflects the value where the mean spacing of dislocations (~100 nm) is approximately equal to the electron-material interaction depth, and thus is near the single dislocation limit. Further exploration of the trends in contrast at lower dislocation densities require more sophisticated dynamical diffraction simulations.

To directly test this concept, we firstly examined the pattern sharpness of two experimental patterns that are near to and away from a dislocation cell wall, yet within the same grain in the SLM 316L SS sample (Fig. 2). Both patterns were subjected to the same pre-processing, including background subtraction and histogram equalization. Since the two patterns are from the same grain, they show qualitatively the same Kikuchi bands that are not distinguishable by eye. The distinction is more obvious in the corresponding logarithmic power spectra in Fig. 2 (b) and (d). The power spectrum of the second pattern (Fig. 2 (d)) spans a larger area, owing to higher spatial frequency (i.e. sharper) bands being present in the diffraction pattern, as indicated by the larger diameter dashed circle as compared with the power spectrum of the first pattern (Fig. 2 (b)). This result indicates that the pattern collected far away from dislocation cell wall in Fig. 2 (c) is a sharper pattern than its counterpart in (a), or equivalently, that the lower sharpness reflects the strain field of the dislocations.

Using the pattern sharpness metric, a spatially-resolved sharpness map is generated from an EBSD dataset. A representative sub-grain region of deformed 316L SS is first visualized using crystal orientations (Fig. 3(a). Both dislocation cell structures and low angle boundaries are readily observed in the pattern sharpness map (Fig. 3(b)); thus, both GNDs and SSDs

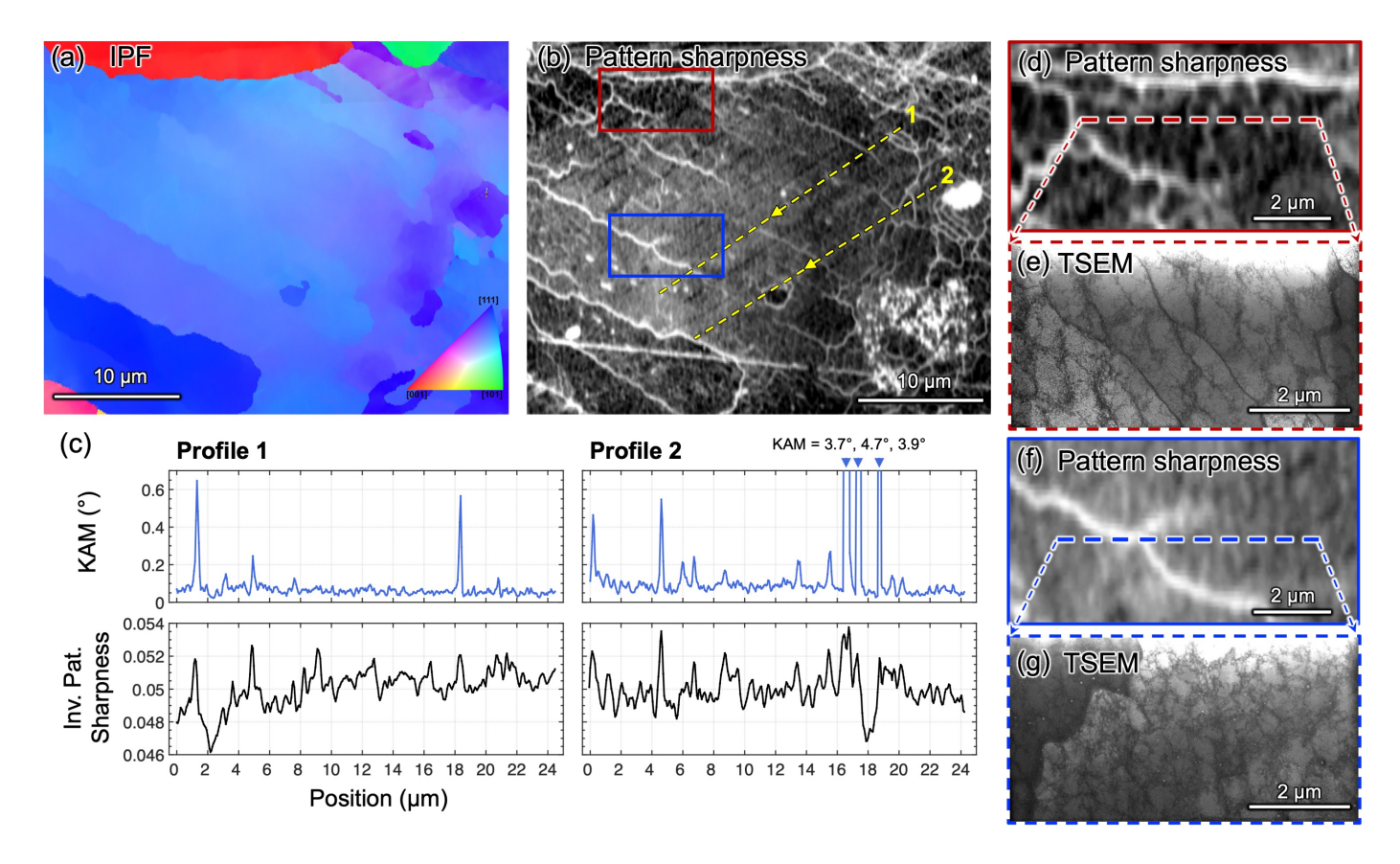


Figure 3: (a) IPF map of a subgrain region from an EBSD dataset collected from a deformed sample of 316L SS. (b) Inverse pattern sharpness map over the exact region from (a), with bright features reflecting low pattern sharpness and high dislocation density, and dark regions representing high pattern sharpness and low dislocation density. Sub-grain features such as low angle boundaries and dislocation cells are readily observed. (c) Line profiles of KAM and inverse pattern sharpness along the two dashed yellow lines in (c). (d, f) Magnified regions of the pattern sharpness map in (b) indicated by red and blue boxes. (e) and (g) are TSEM images of the FIB cross-section lift-out foils from the red and blue dashed lines in (d) and (f), respectively.

comprising the total dislocation content are reflected in pattern sharpness. The contrast of the map is inverted for easy visualization, i.e. a white pixel corresponds to low sharpness of the pattern. A clear benefit of the sharpness metric is the ability to resolve the dislocation cells in most, if not all, of the subgrain regions, which is not directly possible by other techniques such as ECCI without tilting to maintain diffraction contrast. Furthermore, the cell walls appear to have different intensity contrast in the map. In light of the postulate [26] that EBSD pattern sharpness is correlated to dislocation density in the diffracting volume, the varying contrast in the sharpness map could be suggestive of varying local dislocation density or the extent of dislocation entanglement, or chemical segregation - as will be discussed later. To test these concepts, magnified views of two regions (red and blue boxes in Fig. 3(b)) of the pattern sharpness map are shown in Fig. 3(d) and (f). The region in Fig. 3(d) shows low angle boundaries and well defined dislocation cells with high contrast. By comparison, the region in Fig. 3(f) shows a more uniform background intensity in the vicinity of a low angle boundary, suggesting a more uniform dislocation microstructure. To link the pattern sharpness details to the underlying sub-surface dislocation structure, two foils were extracted by focused ion beam (FIB) cross-section lift-out from the two regions (Fig. 3(e) and (f)). The foils were imaged using the transmission mode in SEM (TSEM) [27]. Indeed, direct comparison of the dislocation structure immediately subsurface of the specimen proves that the high contrast region in the sharpness map corresponds to more organized dislocation cell walls with minimal intra-cellecular dislocation content (Fig. 3(e)), so there is a clearer distinction between volumes of high and low dislocation density. In contrast, the low contrast region with an overall increased background intensity in the sharpness map corresponds to more diffuse cell walls (Fig. 3(f)), where the less tangled dislocations spread into cell interiors. Additionally, the thin foil in Fig. 3(f) is separated into two regions of distinct diffraction conditions by a low angle boundary, and such a boundary appears as a thicker white line that crosses the blue dashed line in the sharpness map, indicating high dislocation density in the boundary compared with other cell walls. These results indicate that pattern sharpness is inherently linked to the total dislocation content and can reveal the fine details of defected microstructures arising from both solidification and deformation of additively manufactured materials.

Since both the pattern sharpness and indexed orientation data modalities are based on the same EBSD scan dataset, the maps are naturally correlated without the need of imaging distortion correction or feature tracking, as is necessary when correlating secondary or backscatter electron images with EBSD maps [28]. Therefore, quantitative information about the dislocation cells can be readily obtained, e.g. when correlating pattern sharpness and KAM profiles as in Fig. $\boxed{3}$ (d). Acknowledging that low pattern sharpness is related to high dislocation density, the peaks in the profile of inverse pattern sharpness correspond to cell walls, then an average cell size is obtained, as 856±296 nm along profile 1 and 852±336 nm along profile 2. The values are comparable to those obtained from direct imaging (e.g. TSEM images in Fig. $\boxed{3}$ (e, g)). Comparison of the peaks in the KAM and inverse pattern sharpness profiles shows that most cell walls possess a misorientation smaller than 0.3° over a distance of 24 μm. Similar observations have also been obtained in a single grain contained in a TEM thin foil of SLM 316L SS $\boxed{4}$, where the misorientation at cell walls was approximately 0.5° to 1°.

The pattern sharpness analysis is further applied to scan datasets from other polycrystalline AM materials. In Fig. 4, the microstructure maps of the three printed alloys are presented using different parameters. Pattern sharpness maps are evidently advantageous over the Hough IQ maps in revealing the dislocation cell structures in all the grains. This is primarily because the Hough IQ is affected by the brightness of the diffraction pattern that is also dependent on crystal orientation. As highlighted in Fig. 4, the grains G1, G2 and G3 are overall brighter in the Hough IQ map, thereby obscuring any dislocation cells within them. In contrast, pattern sharpness is obtained from the broadening of the Kikuchi bands (calculated from the power spectrum), reflecting features in the frequency domain, not the diffraction intensity. Simply speaking, pattern sharpness is an orientation-insensitive imaging metric that directly identifies crystalline defects, with an added simplicity for multi-grain imaging compared with ECCI.

Examination of the KAM and pattern sharpness maps reveals distinct features of the cell walls in the three printed alloys. Consistent with the observations in Fig. 3, the KAM map of SLM 316L SS does not clearly delineate any boundaries, despite the profuse dislocation cells as shown by the sharpness map. These cell walls, thus, are not boundaries that accommodate different crystal orientations. In contrast, for the SLM superalloys, Inconel 625 and SB-CoNi-10, the KAM maps contain clear boundaries, and they all coincide with the cell walls. Therefore, conclusions can be drawn regarding the nature of the dislocation cells, at least for these three printed alloys here, that the cell walls in 316L SS contain largely statistically stored dislocations (SSD) that do not possess a noticeable net misorientation, whereas the cell walls in the two superalloys contain largely geometrically necessary dislocations (GND).

The different natures of the dislocation cells in different materials, and presumably at different printing conditions, shed light on the origin of the profusely observed dislocation cells and their effect on the mechanical properties. While dedicated studies are necessary to obtain a deeper understanding, the following hypotheses are put forward. Regarding the formation of dislocation cells during AM, several origins have been suggested in literature, including the merging of dendrites at different orientations, thermoelastic distortion (including shrinkage) stresses by the solidified material surrounding the melt

pool, repeated thermal cycling of the printed volume, and internal stresses due to solute segregation and particles [9, 29–31]. These processes are expected to produce different types of dislocations. For instance, the merging of dendrites may create GND walls, and thermal cycling involves forward and backward dislocation motion and therefore may form dislocation cells akin to those after cyclic loading. An et al. [32] revealed that the cell walls in a TRIP steel after cyclic loading are composed of dislocation dipoles that overall do not have an appreciable misorientation. In this regard, the low KAM values of the cell walls in SLM 316 SS shown here seem to imply that these cells are formed by the entanglement of gliding dislocations driven by cyclic thermal stresses.

The nature of the cell walls, being primarily SSDs or GNDs, suggests that appropriate theoretical models should be chosen when evaluating their effect on mechanical properties. Firstly, the measurement of dislocation density would be affected by the different types of dislocation cells. The cells in SLM 316L SS that do not possess appreciable misorientation gradients would not be captured by GND calculations, which was demonstrated by the measurements in [5] that GND only accounts for about half of the total dislocation density in the same material. This leads to a question of how potent dislocation cells are as dislocation slip obstacles. Whereas SLM 316L SS possesses the attractive properties of having favorable ductility and enhanced hardening in the as-printed state than its counterpart produced by conventional methods [4,5], SLM Inconel 718 was shown to have lower yield stress than the wrought counterpart in the standard heat treatment condition [31]. Detailed characterization of the profuse dislocation cells may be an avenue for elucidating their contribution in strengthening and hardening.

Another factor to be considered in future pattern sharpness analysis on AM materials is the impact of solute segregation, which is observed at the cell walls in materials such at 316L [8], and could amplify or reduce the strain field and therefore the pattern sharpness. Likely, deconvolution of the strain contribution of dislocations (of various types) and segregated solute atoms would require multi-physics simulations, presumably including Scheil analysis for the amount of segregated atoms, phase field simulation for their spatial distribution [33], solute-dislocation interaction models to obtain the net strain field [34], and dynamical EBSD simulations to evaluation the effect on the diffraction patterns.

4. Conclusions

In summary, the EBSD pattern sharpness metric is effective in revealing ensembles of dislocations, such as dislocation cells generated from AM in the present study, and more generally in complex deformed microstructures in bulk specimens. This metric is especially advantageous for characterizing the spatial arrangement of dislocations cells and variation of dislocation density across regions of different orientations. Since the underlying diffraction information used to compute pattern sharpness is generated along with other modalities from the same EBSD dataset, this approach could play an important role in establishing correlative, statistical and even quantitative descrip-

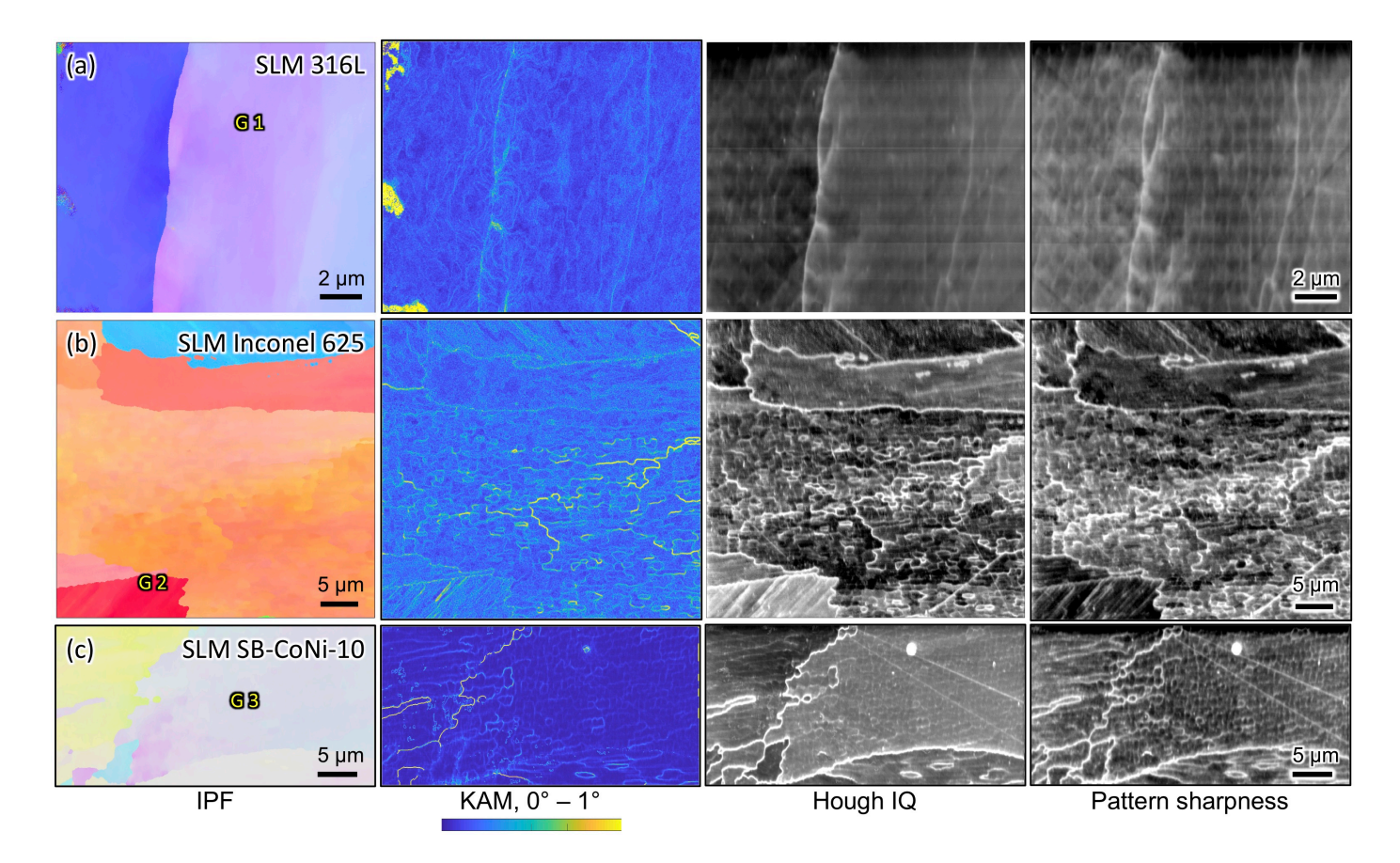


Figure 4: EBSD orientation-based maps (IPF and KAM maps), and EBSD pattern-based maps (Hough image quality and pattern sharpness maps) of (a) SLM 316L SS deformed in tension to 1%, (b) SLM Inconel 625 and (c) SLM SB-CoNi-10 alloys. The Hough IQ and pattern sharpness maps are inverted, with the dark pixel intensity representing high IQ and high sharpness values. The data were acquired on Hikari Plus EBSD detector, using an accelerating voltage of 30 kV, beam current 5.53nA, and scan step size 20 nm.

tions (with the aid of dislocation-sensitive dynamical electron diffraction simulations) of dislocation structures. Practically, pattern sharpness as obtained using standard EBSD equipment and widely available software could pave the path for full-field defect characterization at the mesoscale. Advanced detectors offering high electron detection sensitivity could further unlock additional details of the dislocation attributes [16, 35], and represents an interesting area for future research.

Declaration of Competing Interest

The authors declare that they have no known competing financial interests or personal relationships that could have appeared to influence the work reported in this paper.

Acknowledgements

This work was supported by the Materials Research Science and Engineering Center (MRSEC) program of the National Science Foundation (NSF) through DMR-1720256 (IRG-1), and employed the shared facilities of the MRSEC at UC Santa Barbara, a member of the Materials Research Facilities Network. We also acknowledge support from the Major Research Instrumentation Awards NSF DMR-1828628 and DMR-2117843.

Use was made of the computational facilities administered by the Center for Scientific Computing at the CNSI and MRL (an NSF MRSEC; DMR-1720256) and purchased through NSF CNS-1725797. Furthermore, GPU resources through NSF CC* Compute 1925717 were also leveraged. F. Wang is sponsored by Shanghai Pujiang Program (No. 21PJ1406700). MDG acknowledges funding from a DoD Vannevar-Bush Faculty Fellowship (N00014-16-1-2821). We thank Benjamin Bammes and Barnaby Levin (Direct Electron) for instrument support and fruitful discussions.

References

- [1] J. H. Martin, B. Yahata, J. Mayer, R. Mone, E. Stonkevitch, J. Miller, M. R. O'Masta, T. Schaedler, J. Hundley, P. Callahan, T. Pollock, Grain refinement mechanisms in additively manufactured nano-functionalized aluminum, Acta Materialia 200 (2020) 1022-1037. doi:https://doi.org/10.1016/j.actamat.2020.09.043
 URL https://www.sciencedirect.com/science/article/pii/S1359645420307370
- [2] A. T. Polonsky, N. Raghavan, M. P. Echlin, M. M. Kirka, R. R. Dehoff, T. M. Pollock, Scan strategies in EBM-printed IN718 and the physics of bulk 3d microstructure development, Materials Characterization 190 (2022) 112043. doi:10.1016/j.matchar.2022.112043 URL https://doi.org/10.1016/j.matchar.2022.112043
- [3] A. T. Polonsky, W. C. Lenthe, M. P. Echlin, V. Livescu, G. T. Gray, T. M. Pollock, [Solidification-driven orientation gradients in additively]

- manufactured stainless steel, Acta Materialia 183 (2020) 249–260. doi: 10.1016/j.actamat.2019.10.047
- URL https://doi.org/10.1016/j.actamat.2019.10.047
- [4] Y. M. Wang, T. Voisin, J. T. McKeown, J. Ye, N. P. Calta, Z. Li, Z. Zeng, Y. Zhang, W. Chen, T. T. Roehling, R. T. Ott, M. K. Santala, P. J. Depond, M. J. Matthews, A. V. Hamza, T. Zhu, Additively manufactured hierarchical stainless steels with high strength and ductility, Nature Materials 17 (1) (2018) 63–71. doi:10.1038/nmat5021
 URL https://doi.org/10.1038/nmat5021
- [5] M. Shamsujjoha, S. R. Agnew, J. M. Fitz-Gerald, W. R. Moore, T. A. Newman, High strength and ductility of additively manufactured 316l stainless steel explained, Metallurgical and Materials Transactions A 49 (7) (2018) 3011–3027. doi:10.1007/s11661-018-4607-2 URL https://doi.org/10.1007/s11661-018-4607-2
- [6] Z. Li, B. He, Q. Guo, Strengthening and hardening mechanisms of additively manufactured stainless steels: The role of cell sizes, Scripta Materialia 177 (2020) 17–21. doi:https://doi.org/10.1016/j.scriptamat.2019.10.005
 - URL https://www.sciencedirect.com/science/article/pii/ S1359646219305883
- [7] X. Wang, B. Zheng, K. Yu, S. Jiang, E. J. Lavernia, J. M. Schoenung, The role of cell boundary orientation on mechanical behavior: A site-specific micro-pillar characterization study. Additive Manufacturing 46 (2021) 102154. doi:https://doi.org/10.1016/j.addma.2021.102154. URL https://www.sciencedirect.com/science/article/pii/S2214860421003183
- [8] S.-H. Li, Y. Zhao, P. Kumar, U. Ramamurty, Effect of initial dislocation density on the plastic deformation response of 316l stainless steel manufactured by directed energy deposition. Materials Science and Engineering: A 851 (2022) 143591. doi:10.1016/j.msea.2022.143591. URL https://doi.org/10.1016/j.msea.2022.143591.
- K. Bertsch, G. Meric de Bellefon, B. Kuehl, D. Thoma, Origin of dislocation structures in an additively manufactured austenitic stainless steel 316l, Acta Materialia 199 (2020) 19-33. doi:https://doi.org/10.1016/j.actamat.2020.07.063
 URL https://www.sciencedirect.com/science/article/pii/S1359645420305796
- [10] M. Godec, S. Zaefferer, B. Podgornik, M. Å inko, E. Tchernychova, Quantitative multiscale correlative microstructure analysis of additive manufacturing of stainless steel 316l processed by selective laser melting, Materials Characterization 160 (2020) 110074. doi:https://doi. org/10.1016/j.matchar.2019.110074 URL https://www.sciencedirect.com/science/article/pii/ S1044580319326749
- [11] W. A. Witzen, A. T. Polonsky, T. M. Pollock, I. J. Beyerlein, Three-dimensional maps of geometrically necessary dislocation densities in additively manufactured ni-based superalloy IN718, International Journal of Plasticity 131 (2020) 102709, doi:10.1016/j.ijplas.2020.102709

 URL https://doi.org/10.1016/j.ijplas.2020.102709
- [12] D. B. Menasche, W. D. Musinski, M. Obstalecki, M. N. Shah, S. P. Donegan, J. V. Bernier, P. Kenesei, J.-S. Park, P. A. Shade, AFRL additive manufacturing modeling series: Challenge 4, in situ mechanical test of an IN625 sample with concurrent high-energy diffraction microscopy characterization, Integrating Materials and Manufacturing Innovation 10 (3) (2021) 338–347. doi:10.1007/s40192-021-00218-3 URL https://doi.org/10.1007/s40192-021-00218-3
- [13] M. G. Chapman, M. N. Shah, S. P. Donegan, J. M. Scott, P. A. Shade, D. Menasche, M. D. Uchic, AFRL additive manufacturing modeling series: Challenge 4, 3d reconstruction of an IN625 high-energy diffraction microscopy sample using multi-modal serial sectioning. Integrating Materials and Manufacturing Innovation 10 (2) (2021) 129–141. doi:10.1007/s40192-021-00212-9
 URL https://doi.org/10.1007/s40192-021-00212-9
- [14] S. P. Murray, K. M. Pusch, A. T. Polonsky, C. J. Torbet, G. G. E. Seward, N. Zhou, S. A. J. Forsik, P. Nandwana, M. M. Kirka, R. R. Dehoff, W. E. Slye, T. M. Pollock, A defect-resistant co-ni superalloy for 3d printing, Nature Communications 11 (1) (Oct. 2020). doi: 10.1038/s41467-020-18775-0
 URL https://doi.org/10.1038/s41467-020-18775-0
- [15] J. Rossin, B. Goodlet, C. Torbet, W. Musinski, M. Cox, J. Miller, M. Groeber, A. Mayes, E. Biedermann, S. Smith, S. Daly, T. Pollock,

- Assessment of grain structure evolution with resonant ultrasound spectroscopy in additively manufactured nickel alloys Materials Characterization 167 (2020) 110501. doi:10.1016/j.matchar.2020.110501 URL https://doi.org/10.1016/j.matchar.2020.110501
- [16] F. Wang, M. P. Echlin, A. A. Taylor, J. Shin, B. Bammes, B. D. Levin, M. De Graef, T. M. Pollock, D. S. Gianola, Electron backscattered diffraction using a new monolithic direct detector: High resolution and fast acquisition, Ultramicroscopy 220 (2021) 113160. doi:https://doi.org/10.1016/j.ultramic.2020.113160. URL https://www.sciencedirect.com/science/article/pii/S030439912030303X
- [17] N. C. K. Lassen, Automated determination of crystal orientations from electron backscattering patterns, Ph.D. thesis, Department of Mathematical Modelling, Technical University of Denmark, DTU, Richard Petersens Plads, Building 321, DK-2800 Kgs. Lyngby (1994). URL http://www2.compute.dtu.dk/pubdb/pubs/1200-full.
- [18] M. De Graef, M. A. Jackson, J. Kleingers, C. Zhu, J. Tessmer, W. C. Lenthe, S. Singh, M. Atkinson, S. I. Wright, H. Ånes, Emsoft-org/emsoft: Emsoft release 5.0.0 (2019). doi:10.5281/ZENODO.3489720. URL https://zenodo.org/record/3489720
- [19] W. C. Lenthe, S. Singh, M. De Graef, A spherical harmonic transform approach to the indexing of electron back-scattered diffraction patterns, Ultramicroscopy 207 (2019) 112841. doi:10.1016/j.ultramic.2019. 112841
 URL https://doi.org/10.1016/j.ultramic.2019.112841
- [20] H. W. Ånes, L. Lervik, Onatlandsmyr, T. Bergh, Z. Xu, E. Prestat, pyxem/kikuchipy: kikuchipy 0.6.1 (2022). doi:10.5281/ZENODO. 6655562 URL https://zenodo.org/record/6655562
- [21] S. I. Wright, M. M. Nowell, D. P. Field, A review of strain analysis using electron backscatter diffraction, Microscopy and Microanalysis 17 (3) (2011) 316–329. doi:10.1017/s1431927611000055 URL https://doi.org/10.1017/s1431927611000055
- [22] N. Krieger Lassen, D. Juul Jensen, K. Conradsen, Image processing procedures for analysis of electron back scattering patterns, Scanning Microscopy 6 (1) (1992) 7. URL https://digitalcommons.usu.edu/microscopy/vol6/ iss1/7
- [23] S. I. Wright, M. M. Nowell, EBSD image quality mapping, Microscopy and Microanalysis 12 (01) (2005) 72–84. doi:10.1017/s1431927606060090.
 URL https://doi.org/10.1017/s1431927606060090
- [24] T. Ungar, J. Gubicza, G. Ribarik, A. Borbely, Crystallite size distribution and dislocation structure determined by diffraction profile analysis: principles and practical application to cubic and hexagonal crystals, Journal of Applied Crystallography 34 (3) (2001) 298–310. doi: 10.1107/S0021889801003715

 URL https://doi.org/10.1107/S0021889801003715
- [25] T. Ungar, Microstructural parameters from x-ray diffraction peak broadening. Scripta Materialia 51 (8) (2004) 777-781, viewpoint set no. 35. Metals and alloys with a structural scale from the micrometer to the atomic dimensions. doi:https://doi.org/10.1016/j.scriptamat.2004.05.007.
 URL https://www.sciencedirect.com/science/article/pii/S1359646204002738
- [26] C. Zhu, M. De Graef, Ebsd pattern simulations for an interaction volume containing lattice defects. Ultramicroscopy 218 (2020) 113088. doi: https://doi.org/10.1016/j.ultramic.2020.113088. URL https://www.sciencedirect.com/science/article/pii/S0304399120302394
- [27] P. G. Callahan, J. C. Stinville, E. R. Yao, M. P. Echlin, M. S. Titus, M. De Graef, D. S. Gianola, T. M. Pollock, Transmission scanning electron microscopy: Defect observations and image simulations, Ultramicroscopy 186 (2018) 49 61. doi:https://doi.org/10.1016/j.ultramic.2017.11.004 URL http://www.sciencedirect.com/science/article/pii/S0304399117303315
- [28] M. Charpagne, J. C. Stinville, A. T. Polonsky, M. P. Echlin, T. M. Pollock, A multi-modal data merging framework for correlative investigation of strain localization in three dimensions, JOM 73 (11) (2021) 3263–3271.

- doi:10.1007/s11837-021-04894-6
- URL https://doi.org/10.1007/s11837-021-04894-6
- [29] V. S. Zolotorevsky, N. A. Belov, M. V. Glazoff, Chapter two structure and microstructure of aluminum alloys in as-cast state, in: V. S. Zolotorevsky, N. A. Belov, M. V. Glazoff (Eds.), Casting Aluminum Alloys, Elsevier, Amsterdam, 2007, pp. 95–182. doi:https://doi.org/10.1016/B978-008045370-5.50004-3
 URL https://www.sciencedirect.com/science/article/pii/
 - URL https://www.sciencedirect.com/science/article/pii/B9780080453705500043
- [30] A. J. Birnbaum, J. C. Steuben, E. J. Barrick, A. P. Iliopoulos, J. G. Michopoulos, Intrinsic strain aging, Σ3 boundaries, and origins of cellular substructure in additively manufactured 316l Additive Manufacturing 29 (2019) 100784. doi:https://doi.org/10.1016/j.addma. 2019.100784.
 - URL https://www.sciencedirect.com/science/article/pii/ S2214860419303811
- [31] T. G. Gallmeyer, S. Moorthy, B. B. Kappes, M. J. Mills, B. Amin-Ahmadi, A. P. Stebner, Knowledge of process-structure-property relationships to engineer better heat treatments for laser powder bed fusion additive manufactured inconel 718, Additive Manufacturing 31 (2020) 100977. doi:https://doi.org/10.1016/j.addma.2019.100977. URL https://www.sciencedirect.com/science/article/pii/S2214860419314538
- [32] D. An, S. Zaefferer, Formation mechanism of dislocation patterns under low cycle fatigue of a high-manganese austenitic trip steel with dominating planar slip mode. International Journal of Plasticity 121 (2019) 244– 260. doi:https://doi.org/10.1016/j.ijplas.2019.06.009. URL https://www.sciencedirect.com/science/article/pii/ S0749641919300440
- [33] T. Keller, G. Lindwall, S. Ghosh, L. Ma, B. M. Lane, F. Zhang, U. R. Kattner, E. A. Lass, J. C. Heigel, Y. Idell, M. E. Williams, A. J. Allen, J. E. Guyer, L. E. Levine, Application of finite element, phase-field, and calphad-based methods to additive manufacturing of ni-based superalloys, Acta Materialia 139 (2017) 244-253. doi:https://doi.org/10.1016/j.actamat.2017.05.003
 URL https://www.sciencedirect.com/science/article/pii/S1359645417303804
- [34] V. Turlo, T. J. Rupert, Linear complexions: Metastable phase formation and coexistence at dislocations, Phys. Rev. Lett. 122 (2019) 126102. doi:10.1103/PhysRevLett.122.126102

 URL https://link.aps.org/doi/10.1103/PhysRevLett.122.126102
- [35] J. Kacher, T. Ruggles, J. Key, M. Nowell, S. Wright, Characterizing defect structures in AM steel using direct electron detection EBSD, Scripta Materialia 221 (2022) 114952. doi:10.1016/j.scriptamat.2022. 114952.
 - URL https://doi.org/10.1016/j.scriptamat.2022.114952